A comparison between the corrosion behavior of 316L stainless steel manufactured by rolling and laser powder bed fusion in 0.1 M H$_2$SO$_4$ solution

H. Ramezanalizadeh*[1], M. Yeganeh*[2], M. H. Rezvani[3], S. M. Lari Baghal[4]

[1] *Department of Materials and Polymer Engineering, Faculty of Engineering, Hakim Sabzevari University, P.O. Box 397, Sabzevar, Iran*

[2,3,4] *Department of Materials Science and Engineering, Faculty of Engineering, Shahid Chamran University of Ahvaz, Ahvaz, Iran*

Abstract

Recently, laser powder bed fusion (LPBF) technology as an important additive manufacturing (AM) technique has attracted the attention of researchers. It uses a laser source to melt metal powder in layers in order to build parts. In this study, electrochemical and surface properties of 316L stainless steel manufactured by rolling and laser powder bed fusion (LPBF) were investigated in 0.1 M H$_2$SO$_4$ solution. In order to examine the corrosion behavior of stainless steel in an acidic medium, electrochemical methods, including electrochemical impedance spectroscopy (EIS), potentiodynamic polarization, and characterization methods such as field emission scanning electron microscopy (FESEM), and x-ray photoelectron spectroscopy (XPS), were used. As a result of the electrochemical tests, the charge transfer resistance of stainless steel fabricated by LPBF increased about 8 times and Ecorr shifted about +40 mV compared to the rolled stainless steel. LPBF-produced samples had higher corrosion resistance due to the fine cellular and spherical inclusion microstructure formed during the fabrication process.

Keywords: Laser powder bed fusion (LPBF); 316L stainless steel; H$_2$SO$_4$ corrosion; Passive layer.

1. Introduction

In additive manufacturing (AM), laser powder bed fusion (LPBF) is an important technique. In this method, in order to build parts, metal powder is melted by a laser source [1,2]. In comparison to other non-powder bed-based laser systems like engineered net shaping (LENS),

*Corresponding author
Email: h.ramezanalizadeh@hsu.ac.ir, m.yeganeh@scu.ac.ir
Address: Department of Materials and Polymer Engineering, Faculty of Engineering, Hakim Sabzevari University, P.O. Box 397, Sabzevar, Iran
Department of Materials Science and Engineering, Faculty of Engineering, Shahid Chamran University of Ahvaz, Ahvaz, Iran
1. Assistant Professor
2. Assistant Professor
3. MSc Student
4. Assistant Professor

LPBF has the advantage of building complex geometries with high resolution and accuracy. Stainless steel alloys have outstanding mechanical and corrosion properties, which makes AM methods a good choice for making these alloys [3]. 316L stainless steel (SS) has numerous excellent properties besides its excellent properties as a stainless steel alloy, such as high resistance to cutting, high ductility, high sensitivity to grain boundary corrosion after welding, and low heat conductivity [4,5]. As a result of these properties, these alloys are ideal for additive manufacturing, especially with near-net-shape pieces for many industries and applications [6–8].

Additionally, LPBF products are capable of achieving full density and have comparable mechanical properties with respect to conventional methods [9,10]. In contrast to conventional castings or wrought metals, the process provides a unique microstructure with a cooling rate of 10^3-10^8 Ks^{-1} [11]. At the macro-scale, the LPBF process produces overlapping melt pools that appear circle-like in the direction of the building. Moreover, LPBF-

manufactured 316L stainless steel is characterized by a cellular/columnar microstructure. These sub-grain boundaries have a very fine microstructure [12,13].

A broad range of feedstock used in the LPBF method is steel alloys. 316L stainless steel (316L SS) as a steel alloy has been widely LPBF-produced due to its great weldability [14,15]. By contrast, 316L stainless steel manufactured by LPBF has a significantly different microstructure from steel manufactured by conventional methods. Microstructural characteristics of laser-melted alloys include clearly visible melt pool boundaries [16,17]. LPBF 316L SS usually has a hierarchical microstructure of cellular/columnar grains with fine inclusions, resulting in excellent mechanical properties, ductility, or corrosion resistance [17,18]. 316L stainless steel is suitable for nuclear systems, aerospace devices, chemical reactors, marine vessels, pipes, and biomedical devices such as implants, orthopedics, and dentistry, due to its low cost, good mechanical performance, and excellent corrosion resistance [14,19–21].

An increasing number of researchers have been interested in studying the corrosion resistance of LPBF-fabricated 316L stainless steel. According to some researchers, additive manufactured 316L stainless steel has more corrosion resistant than conventional stainless steel [22,23]. They believed the higher corrosion behavior of the AM 316L SS sample is related to the ultrafine grain structure due to the rapid quenching of the laser-melted alloy powders [24]. In addition, Stainless steel passive film with fine cellular/columnar structure could be more stable in corrosive media [25-27]. In some cases, it was reported that LPBF-processed 316L stainless steel exhibits lower corrosion resistance than the wrought counterpart due to its complex microstructure or the possibility of defects formation in the LPBF-produced pieces [28–30]. This is due to the segregation of some elements like Mo at the boundaries, so that the microstructure becomes inhomogeneous, and as a consequence, the corrosion resistance of LPBF samples decreases compared to their conventional counterparts [28]. Furthermore, the formed porosity during the laser fabrication could behave as the pitting initiation sites in the case of LPBF 316L stainless steel [22]. Under different aggressiveness solutions, Duan et al. [31] compared pitting behaviors between wrought stainless steels and LPBF 316L stainless steels. A significant difference was not observed in the shapes of the cyclic polarization curves at different solutions including alkaline pHs, indicating that the two alloys showed comparable electrochemical behavior. The corrosion behavior of LPBF 316L stainless steel alloy in the concrete pore solutions was investigated by Karimi

et al. [2]. They found that both alloys showed a similar electrochemical response in that alkaline media. LPBF-processed alloy showed slightly better electrochemical behavior, pointing to a more compact passive layer and a lack of sharp edge phases such as TiN [2]. In this study, the corrosion behavior of LPBF-produced 316L SS was evaluated in the sulfuric acid solution using potentiodynamic polarization (PDP), electrochemical impedance spectroscopy (EIS), field emission scanning electron microscopy (FESEM), and x-ray photoelectron spectroscopy (XPS).

2. Materials and methods
2.1. Materials

A pure commercial 316L stainless steel gas atomized powder with an average particle size of 26 μm was used to fabricate the LPBF-manufactured specimen in this work. A fiber laser with a power of 300-watt with a hatch distance (distance between adjacent scan lines) of 100 μm was employed to melt stainless steel powders. The thickness of each melted layer was set ≈30 μm. The optimized parameters were recommended by the system manufacturer (Noura Co. Iran). The LPBF procedure was carried out in a chamber with a high-purity argon gas atmosphere. The cubic samples were manufactured with dimensions of 20 × 20 × 2 mm. Table 1 provides the chemical composition (Quantometer model PMI Master Smart) of rolled and LPBF-processed 316L SS by optical emission quantometer instrument. The analytical grade of H_2SO_4 was obtained from Mojallali Co. Iran without being purified.

2.2. Methods

Roll and LPBF samples were used as the working electrode, a Pt wire as the counter, and a saturated Ag/AgCl electrode as the reference electrode in all electrochemical experiments. The electrochemical analyses were performed by a Radstat 1 potentiostat. For studying the electrochemical activity of specimens in an acidic solution, electrochemical measurements such as electrochemical impedance spectroscopy (EIS) and potentiodynamic polarization were performed. After stabilizing open circuit potential (OCP), EIS measurements were recorded in a frequency range of 10 kHz to 0.1 Hz with an amplitude of the 5 mV AC signal. The corrosion parameters were calculated using ZView software by fitting the experimental results with electrochemical equivalent circuits. Potentiodynamic polarization curves were provided by sweeping the

Table 1. Chemical composition of provided wrought and LPBF-processed 316L SS samples.

Sample	C	Cr	Cu	Al	Si	Mn	Mo	Ni	S	Fe
Roll	0.015	17	0.15	0.007	0.46	1.33	2.1	10.6	0.006	Bal.
LPBF	<0.01	16.9	0.03	0.02	0.61	1.36	2.22	12.1	0.01	Bal.

electrode potential from −0.2 V to +0.2 V vs. OCP at a scan rate of 1 mV.s^{-1}. To approximate polarization parameters such as corrosion current density (i$_{corr}$), corrosion potential (E$_{corr}$), and cathodic and anodic slopes (β$_c$ and β$_a$), the Tafel extrapolation approach was used. To ensure data reproducibility and reliability, electrochemical experiments were replicated at least three times.

After immersion in 0.1 M H$_2$SO$_4$ solution, the chemical surface state of two types of stainless steel was determined by X-ray photoelectron spectroscopy (XPS) using an AlK anode at a 1486.6 eV energy. In the chamber, a vacuum of 1×10^{-10} mBar was applied. Using the calibrated C 1s line at 285.0 eV, binding energy values were determined. SDP v4.0 software was used to fit the peaks with the proper compositions.

3- Results and discussions

Fig. 1 a-d illustrates the FESEM micrographs of the Roll (Fig. 1 a, c) and LPBF (Fig. 1 b, d) 316L SS, respectively. Accordingly, the Rolled alloy displayed typical sharp-edged morphology with equiaxed grain boundaries and a grain size of about 20 microns. LPBF alloy shows a heterogeneous microstructure, which can be observed by other researchers [24]. As a result of the movement of the heat source, the shape of these melt pools is not completely circular. Their length is in the range of 100-200 μm, and their width is between 50-100 μm [32]. Also, the observed cellular/columnar morphology (Fig. 1d) of the alloy can be related to the effect of the high cooling rate during the LPBF process. This special morphology of LPBF alloy shows differences from the traditional 316L stainless steel, which generally has an equiaxed coarse grain structure as discussed in the previous works [2,17,33, 34]. In the FESEM micrographs of the LPBF specimen, ultrafine cellular and columnar sub-grains are observed. This is consistent with grain growth in the direction of heat flow [35]. It is worth mentioning that the size of each cell is dominated by the temperature gradient (G) and the cooling rate (R). In the LPBF process with the high cooling rate, the low ratio of 1/GR provides ultrafine grains [36].

Fig. 1c and Fig. 1d display the presence of inclusions in the Roll and LPBF alloys, respectively. In the Roll sample, the main elements of sharp inclusion are Ti, N, Fe, and Cr, while in the LPBF sample, the main elements are O, Si, Mn, Cr, Fe, and a little Al. Pitting can be initiated by the formation of local cathodes and anodes in the vicinity of the TiN phase. TiN phase can trigger the initiation of pitting due to the formation of local anodes and cathodes [33,37]. The creation of a galvanic couple between the TiN particle and the matrix leads to a destructive effect on the pitting resistance, unlike the TiC particle [37]. However, in the case of the LPBF sample, the main compounds are probably combinations of SiO$_2$,

Cr$_2$O$_3$, Fe$_2$O$_3$, MnO$_2$, and Al$_2$O$_3$ [2,16].

Fig. 2 shows the EDS results for the inclusions in the Roll and LPBF stainless steel alloys. It depicts that the reduction of Cr content from the matrix to the inclusion in the Roll sample is higher than the LPBF sample. Therefore, the local galvanic cell due to the Cr changes between the matrix and inclusion is more favorite in the Roll sample. The appearance of the galvanic cell can be encouraged by the formation of inclusions (as the anodic sites) with the lower Cr content. In other words, low Cr content inclusions can initiate a galvanic cell between themselves and the matrix, accelerating the corrosion damage. Chromium-depleted regions can be considered as the triggers for localized corrosion in stainless steel alloys [26,38].

The variations of open circuit potential (OCP) over time for rolled and LPBF processed 316L SS are illustrated in Fig. 2a. The difference of about 100 mV between the rolled and LPBF processed alloy indicates the higher activity of the rolled sample in the acidic solution compared to LPBF processed counterpart [39]. The variations of OCP towards more negative contents can be evaluated as the depassivation of steel and, or the initiation of localized corrosion [40]. The development of TiN inclusions or α' phase in the rolled alloy could degrade the passive layer or pit nucleation [2].

Nyquist plots of Roll and LPBF samples in 0.1 M H$_2$SO$_4$ are shown in Fig. 2b. Impedance plots present depressed loops indicating the charge transfer resistance of steel as a sign of corrosion performance [41,42]. However, LPBF alloys showed a larger diameter compared to Roll one, indicating the improvement of the corrosion resistance. Moreover, the experimental data were fitted by ZView software to obtain corrosion parameters. The chosen equivalent circuit (EEC model) for data analysis is shown inside Fig. 2b. It is composed of electrolyte resistance (R$_s$), charge transfer resistance (R$_{ct}$), film resistance associated with the passive or oxide layer (R$_o$), and their related constant phase element (CPE$_{ct}$ and CPE$_o$). As a replacement component for capacitance, CPE indicates the system non-homogeneities that results in the depressed appearance of capacitive loops as a result of such physical events as surface roughness and the formation of porous layers [17,41,43]. Table 2 provides the obtained corrosion parameters from fitting the experimental EIS spectra with the equivalent model using ZView software. The charge transfer resistance of the Roll and LPBF samples is 660 and 5150 Ω.cm^2, respectively, indicating that the AM alloy has better corrosion resistance in the sulfuric media. The CPE$_{(ct)}$ and CPE$_{(o)}$ show the values of the relaxed charge through the double layer and the oxide or passive film, respectively [43]. The general reduction of these parameters due to the microstructure variation of LPBF alloy indicates the influence of species adsorption on the steel surface,

leading to the lower corrosion phenomenon [44]. Fig. 2c shows the Bode-Phase plots of the Roll and LPBF 316L stainless steel in the sulfuric acid. As can be observed, the impedance modulus of the LPBF alloy has a higher value compared to the Roll sample in each frequency, indicating better corrosion resistance of this sample in the acidic media. Additionally, the LPBF sample shows a higher phase angle from low to medium frequencies, indicating better stability of the passive film formed on steel [45,46].
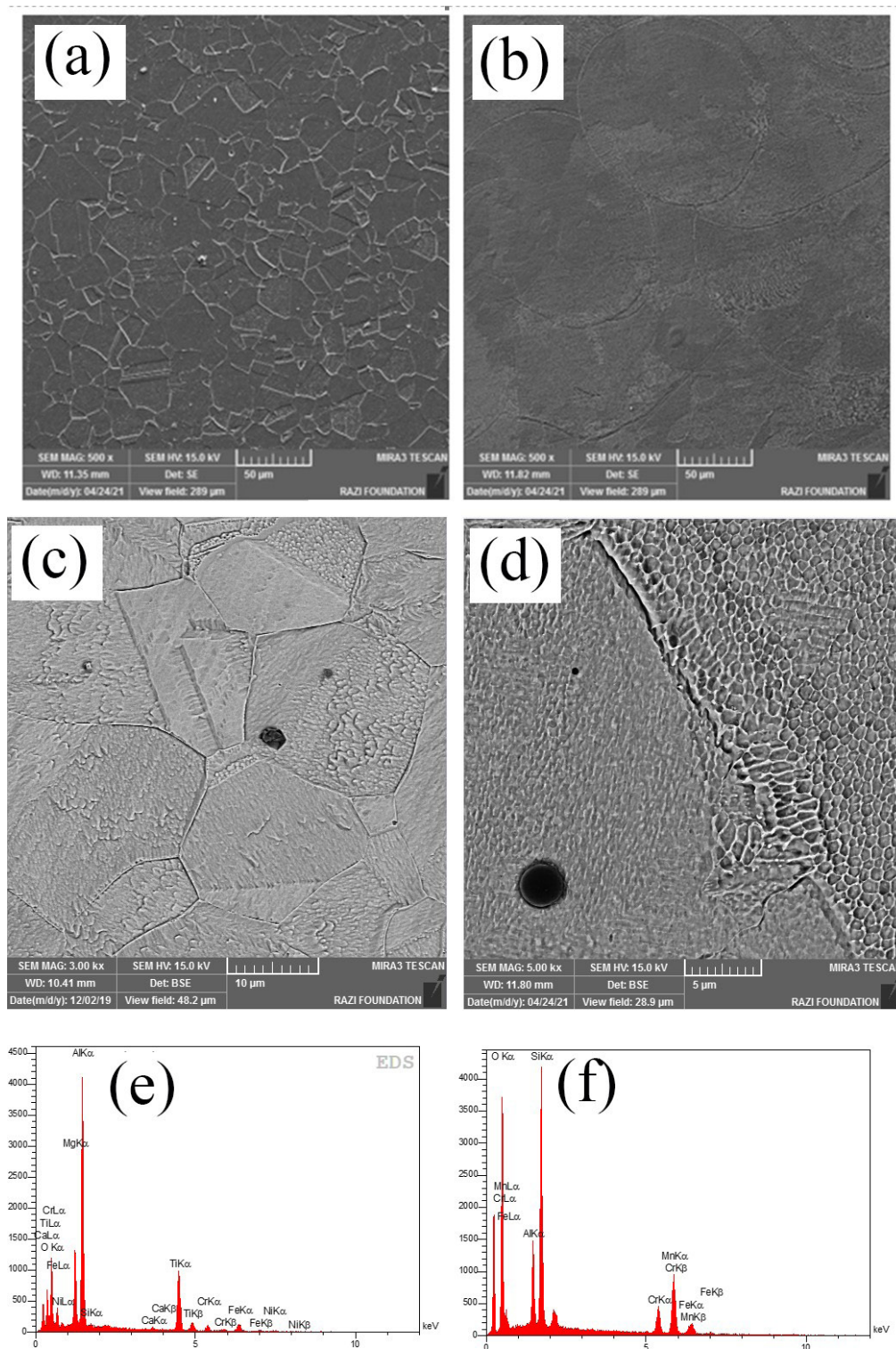

Fig. 1. Secondary electron FESEM micrograph of the (a) Roll and (b) LPBF 316L stainless steel. Back scattered electron FESEM micrographs and EDS related to inclusion in the (c, e) Roll sample, and (d, f) LPBF- processed sample.
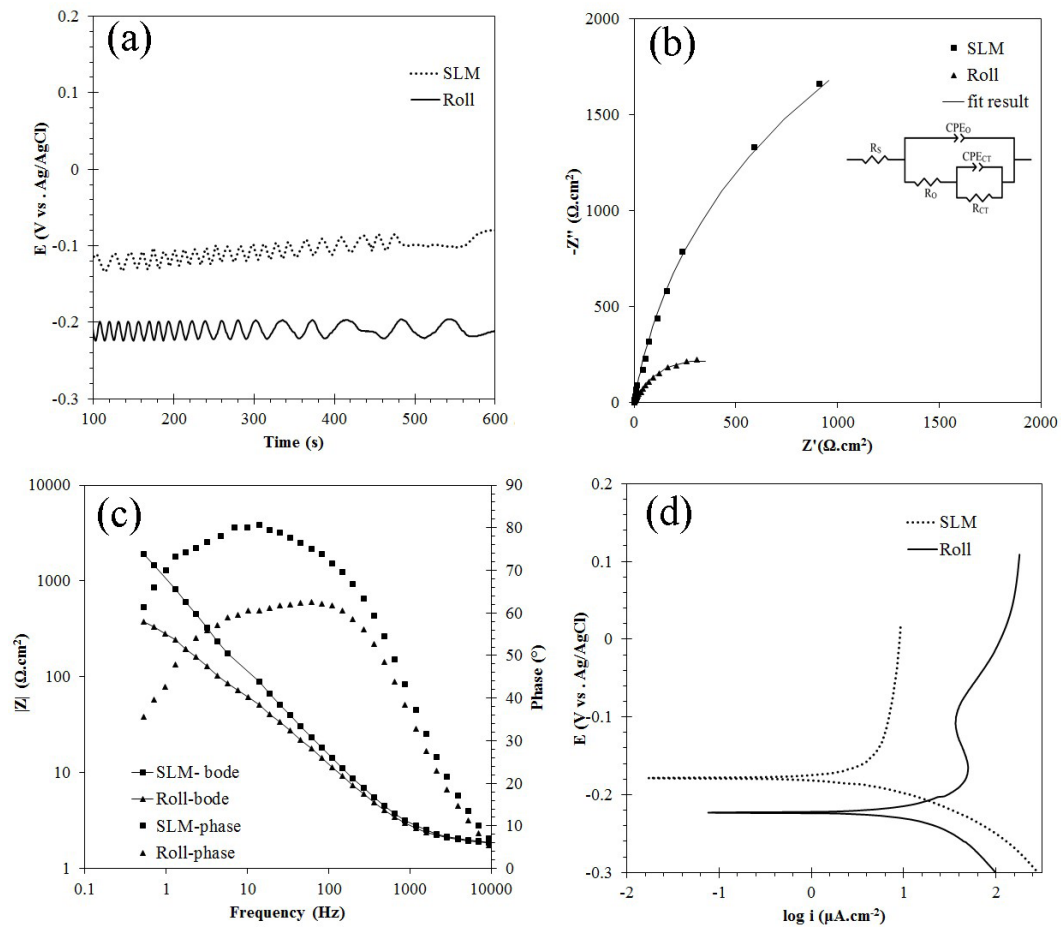
Fig. 2. (a) OCP variations, (b) Nyquist plots, (c) bode plots, and (d) potentiodynamic polarization curves of Roll and LPBF 316L stainless steel in 0.1 M H_2SO_4.

Table 2. The obtained electrochemical parameters obtained from EIS and PDP tests.

sample	CPE(ct), $\mu F\ cm^{-2}\ s^n$	nct	Rct, $\Omega.cm^2$	CPE(o) $\mu F\ cm^{-2}\ s^n$	no	Ro, $\Omega.cm^2$	i_{corr} $(\mu A.cm^{-2})$	E_{corr} (mV vs. Ag/AgCl)	i_{pass} $(\mu A.cm^{-2})$
Roll	200	0.9	660	500	0.95	8	19.6	-225	40.1
LPBF	55	0.92	5150	120	0.91	9.1	2.5	-185	6.5

Fig. 2d depicts potentiodynamic polarization plots of the Roll and LPBF samples in the sulfuric acid media. The corrosion parameters obtained from polarization curves are shown in Table 2, including corrosion current densities (i_{corr}), corrosion potential (E_{corr}), and passivation current density (i_{pass}). As can be observed, the corrosion current density of the LPBF sample is 19.6 $\mu A.cm^{-2}$, while it is 2.5 $\mu A.cm^{-2}$ for the Roll counterpart. In addition, laser manufacturing alters the polarization branches and shifts the E_{corr} to a positive direction in comparison with the Roll sample. This shift toward anodic potentials can be related to the high entrapped energy in the laser-treated microstructure and its tendency to react with sulfuric acid in the anodic potentials. Besides, the polarization curve of LPBF 316L SS alloy does not show the classical passive zones [47], more likely due to different microstructure and elimination of classical grain boundaries which was favored in the traditional alloys. However, a decrease in anodic slope and an increase in cathodic one was observed, which is in contradiction with the literature [44]. Besides, the LPBF sample has lower i_{corr} and i_{pass} compared to the Roll one, which is due to the better corrosion resistance and higher stability of the passive layer.

Fig. 3a-b shows the microstructure of the corroded

surface of the Roll and LPBF alloy after immersion in the 0.1 M H_2SO_4 solution. As can be seen, the surface of Roll alloy possesses a larger pit with an irregular shape. In the Roll sample, the main elements of the corrosion product (A) were 12.1 Fe, 1.5 Cr, 4 Ni, 4.5 Mo, 19 S, and 48 O in wt. %. On the other hand, the major elements of corrosion product (B) in the LPBF sample were 7.4 Fe, 2.7 Mo, 8.7 Cr, 1.9 Mn, 23 Al, and 41 O in wt. %. This indicates the release of Mn and Si from the inclusion during the immersion. It can be concluded that the inclusions in the Roll and LPBF steels can initiate the formation of pits. The formation of pits with a low coherence to the matrix in the Roll sample can be observed. On the other hand, the formed pit in the LPBF sample showed a higher coherency with the matrix.

Fig. 4 shows the high-resolution XPS of Cr 2p, Fe 2p, and O 1s elements in the passive film formed in the H_2SO_4 solution for Roll and LBPF samples. It can be observed that the Fe 2p peaks mainly consist of Fe, FeO, and Fe_2O_3 [17,48,49]. In the case of Cr 2p, Cr_2O_3 in the LPBF alloy has a higher intensity compared to the Roll sample, suggesting better corrosion performance of the laser-manufactured alloy. The O 1s peak in Fig. 4 can be divided into two main peaks, indicating that the oxide film contains oxygen-containing species such as O^{2-} oxide ions and chemisorbed OH^- groups [50]. As can be seen in the O 1s spectrum, the O^{2-}/OH^- intensity ratio in the AM alloy increases sharply. This variation reveals the enhanced hydroxylation of the formed oxide film on the surface of the Roll sample [51]. On the other hand, it can calculate the diameter of oxide thickness (d) according to the literature [52]. d_{LPBF} and d_{Roll} after immersion in the sulfuric acid media are calculated at 1.4 and 1.7 nm, respectively. The formed passive film is a combination of Cr and Fe oxy/hydroxide film on the surface of the samples [48].
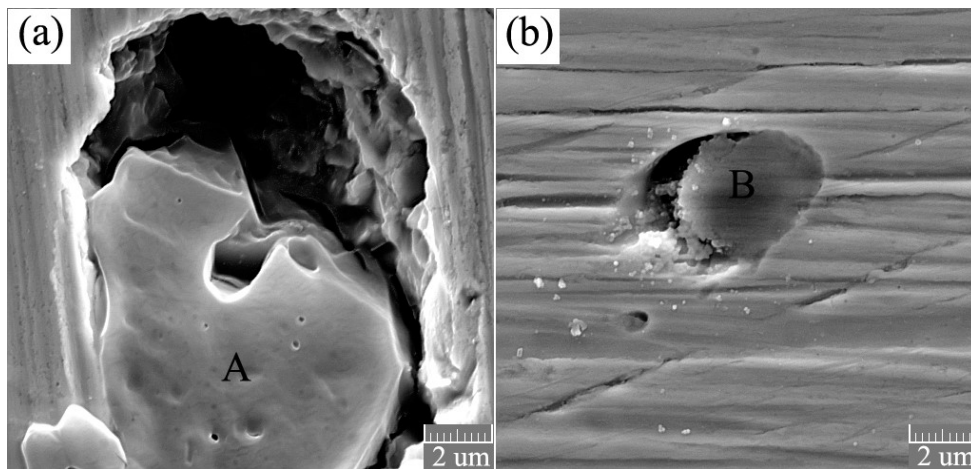

Fig. 3. FESEM micrographs (20 k magnifications) of the (a) Roll and (b) LPBF stainless steel after immersion in the 0.1 M H_2SO_4 solution.
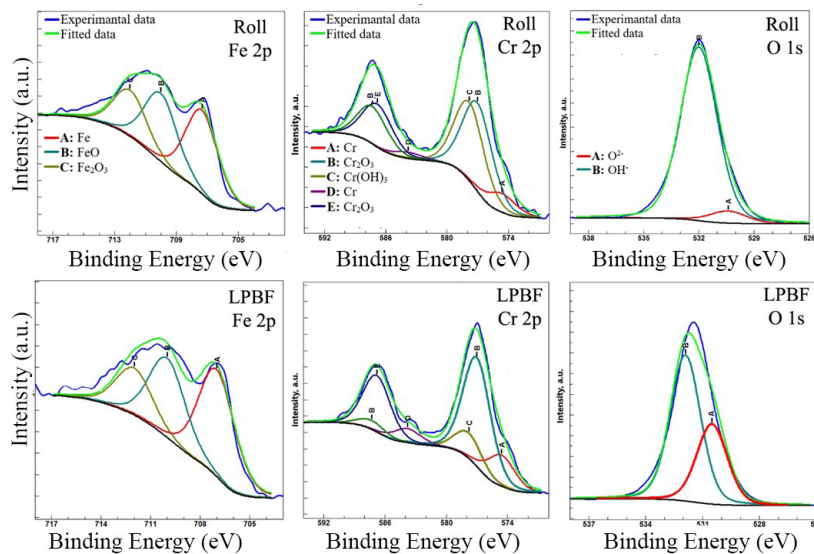

Fig. 4. Spectra of Fe 2p, Cr 2p, and O 1s of passive film formed on the 316L stainless steel in the 0.1 M H_2SO_4.

4- Conclusion

In this study, the corrosion resistance of a rolled and laser powder bed fusion manufactured 316L stainless steel alloy was investigated in the 0.1 M H_2SO_4.

It was found the laser-manufactured alloy showed a lower corrosion current density and higher charge transfer resistance.

The better corrosion resistance of LPBF alloy can be related to the easier formation of the passive layer due to the fine cellular microstructure.

Besides, it was observed that the corrosion pits can initiate from the inclusion in the alloys.

Acknowledgement

References

[1] Z. Sun, X. Tan, S. Tor, W.Y. Yeong, Materials & Design. 104 (2016) 197.

[2] M. H. Shaeri Karimi, M. Yeganeh, S. R. Alavi Zaree, M. Eskandari, Opt Laser Technol. 138 (2021) 106918.

[3] D. Kong, C. Dong, X. Ni, X. Li, npj Mater Degrad. 3 (2019) 1.

[4] M. Kaladhar, K. Venkata Subbaiah, C. H. Srinivasa Rao, Int J Mach Mach Mater. 12 (2012) 178.

[5] Y. Zhao, A. P. Wu, W. Yao, Z. M. Wang, Y. S. Sato, H. Kokawa, Mater Sci Forum. 675–677 (2011) 739.

[6] M. Yakout, M. A. Elbestawi, S. C. Veldhuis, Solid State Phenom. 278 (2018) 1.

[7] F. Bartolomeu, M. Buciumeanu, E. Pinto, N. Alves, O. Carvalho, F. S. Silva, G. Miranda, Addit Manuf. 16 (2017) 81.

[8] F. Andreatta, A. Lanzutti, E. Vaglio, G. Totis, M. Sortino, L. Fedrizzi, Mater Corros. 70 (2019) 1633.

[9] F. Bartolomeu, M. Sampaio, O. Carvalho, E. Pinto, N. Alves, J. R. Gomes, F. S. Silva, G. Miranda J Mech Behav Biomed Mater. 69 (2017) 128.

[10] X. Zhao, Q. Wei, B. Song, Y. Liu, X. Luo, S. Wen, Y. Shi. Mater Manuf Process. 30 (2015) 1283.

[11] B. Song, X. Zhao, S. Li, C. Han, Q. Wei, S. Wen, J. Liu, Y. Shi. Front Mech Eng. 10 (2015) 111.

[12] Y. Zhong, L. Liu, S. Wikman, D. Cui, Z. Shen. J Nucl Mater. 470 (2016) 170.

[13] W. M. Tucho, V. H. Lysne, H. Austbø, A. Sjolyst-Kverneland, V. Hansen. J Alloys Compd. 740 (2018) 910.

[14] K. Lin, D. Gu, L. Xi, L. Yuan, S. Niu, P. Lv, Q. Ge. Int J Adv Manuf Technol. 104 (2019) 2669.

[15] M. Kazemipour, M. Mohammadi, E. Mfoumou, A. M. Nasiri. JOM. 71 (2019) 3230.

[16] K. Saeidi, X. Gao, Y. Zhong, Z. J. Shen. Mater Sci Eng A. 625 (2015) 221.

[17] M. Yeganeh, M. H. Rezvani, S. M. Laribaghal. Colloids Surfaces A Physicochem Eng Asp. 627 (2021) 127120.

[18] Q. Chao, S. Thomas, N. Birbilis, P. Cizek, P. D. Hodgson, D. Fabijanic. Mater Sci Eng A. 821 (2021) 141611.

[19] X. Yue, L. Zhang, Y. Hua, J. Wang, N. Dong, X. Li, S. Xu, A. Neville. Appl Surf Sci. 529 (2020) 147170.

[20] Y. Zhang, F. Liu, J. Chen, Y. Yuan. J Laser Appl. 29 (2017) 022306.

[21] S. Waqar, J. Liu, Q. Sun, K. Guo, J. Sun. Rapid Prototyp J. 26 (2020) 1739.

[22] Q. Chao, V. Cruz, S. Thomas, N. Birbilis, P. Collins, A. Taylor, P. D. Hodgson, D. Fabijanic. Scr Mater. 141 (2017) 94.

[23] M. J. K. Lodhi, K. M. Deen, W. Haider, Materialia. 2 (2018) 111.

[24] M. J. K. Lodhi, K. M. Deen, M. C. Greenlee-Wacker, W. Haider, Addit Manuf. 27 (2019) 8.

[25] S. V. Muley, A. N. Vidvans, G. P. Chaudhari, S. Udainiya, Acta Biomater. 30 (2016) 408.

[26] M. P. Ryan, D. E. Williams, R. J. Chater, B. M. Hutton, D. S. McPhail, Nature. 415 (2002) 770.

[27] C. Ni, Y. Shi, J. Liu, Mater Res Express. 6 (2019) 0865i6.

[28] J. R. Trelewicz, G. P. Halada, O. K. Donaldson, G. Manogharan, Jom. 68 (2016) 850.

[29] D. Kong, X. Ni, C. Dong, L. Zhang, C. Man, J. Yao, K. Xiao, X. Li, Electrochim Acta. 276 (2018) 293.

[30] P. Ganesh, R. Giri, R. Kaul, P. Ram Sankar, P. Tiwari, A. Atulkar, R. K. Porwal, R. K. Dayal, L. M. Kukreja, Mater Des. 39 (2012) 509.

[31] Z. Duan, C. Man, C. Dong, Z. Cui, D. Kong, X. Wang, Corros Sci. 167 (2020) 108520.

[32] D. Gu, Y. C. Hagedorn, W. Meiners, G. Meng, R. J. S. Batista, K. Wissenbach, R. Poprawe, Acta Mater. 60 (2012) 3849.

[33] M. Yeganeh, M. T. Shoushtari, P. Jalali, J Laser Appl. 042001 (2021) 33.

[34] T. Kurzynowski, K. Gruber, W. Stopyra, B. Kuźnicka, E. Chlebus, Mater Sci Eng A. 718 (2018) 64.

[35] L. E. Rännar, A. Koptyug, J. Olsén, K. Saeidi, Z. Shen, Addit Manuf. 17 (2017) 106.

[36] M. C. Flemings, Metall Trans. 5 (1974) 2121.

[37] A. A. Tiamiyu, U. Eduok, J. A. Szpunar, A. G. Odeshi, Sci Rep. 9 (2019)

[38] M. Yeganeh, M. T. Shoushtari, P. Jalali, J Laser Appl. 4 (2021) 042001.

[39] J. T. Pérez-Quiroz, J. Terán, M. J. Herrera, M. Martínez, J. Genescá, J Constr Steel Res. 64 (2008) 1317.

[40] B. Elsener, C. Andrade, J. Gulikers, R. Polder, M. Raupach, Mater Struct. 36 (2003) 461.

[41] M. Saremi, M. Yeganeh, Corros Sci. 86 (2014) 159.

[42] A. Keyvani, M. Yeganeh, H. Rezaeyan, J Mater Eng Perform. 26 (2017) 1958.

[43] M. J. K. Lodhi, K. M. Deen, Z. Ur, A. Farooq, W.

Haider, J Ind Eng Chem. 25 (2018) 180.

[44] M. Yeganeh, I. Khosravi-Bigdeli, M. Eskandari, S. R. A. Zaree, J Mater Eng Perform. 29 (2020) 3983.

[45] D. Kong, C. Dong, X. Ni, L. Zhang, H. Luo, R. Li, L. Wang, C. Man, X. Li, Appl Surf Sci. 504 (2020) 144495.

[46] M. Yeganeh, M. Saremi, Prog Org Coatings. 79 (2015) 25.

[47] J. Zhang, P. Ju, C. Wang, Y. Dun, X. Zhao, Y. Zuo, Y. Tang, Prot Met Phys Chem Surfaces. 55 (2019) 148.

[48] K. M. Deen, M. J. K. Lodhi, E. Asselin, W. Haider, J Phys Chem C. 124 (2020) 21435.

[49] D. G. Li, J. D. Wang, D. R. Chen, Int J Hydrogen Energy. 39 (2014) 20105.

[50] E. McCafferty (2010) Introduction to Corrosion Science, Springer, New York

[51] B. Lynch, F. Wiame, Z. Wang, L. Ma, E. Paschalidou, J Electrochem Soc. 167 (2020) 141509.

[52] A. P. Grosvenor, B. A. Kobe, N. S. McIntyre, S. Tougaard, W. N. Lennard, Surf Interface Anal. 36 (2004) 632.